The evolution of the coronal loop structure due to the phase mixing of high and low-frequency Alfvén waves

H. Callingham [1]★ I. De Moortel[1,2] and P. Pagano[3,4]

[1]*School of Mathematics and Statistics, University of St Andrews, St Andrews, Fife KY16 9SS, UK*
[2]*Rosseland Centre for Solar Physics, University of Oslo, PO Box 1029 Blindern, NO-0315 Oslo, Norway*
[3]*Dipartimento di Fisica & Chimica, Università di Palermo, Piazza del Parlamento 1, I-90134 Palermo, Italy*
[4]*INAF-Osservatorio Astronomico di Palermo, Piazza del Parlamento 1, I-90134 Palermo, Italy*

ABSTRACT

Coronal loops are known to host Alfvén waves propagating in the corona from the lower layers of the solar atmosphere and because of their internal structure, phase mixing is likely to occur. The structure of the coronal loop could be significantly affected by the thermodynamic feedback of the heating generated by phase mixing. However, this phenomenon can be sensitive to the period of the propagating Alfvén waves due to how short period waves can be easily dissipated and the way long-period waves may accumulate considerable energy in resonating coronal loops. Using the LARE2D code, a coronal loop model of a field-aligned thermodynamic equilibrium and a cross-field background heating profile is created, with an additional forcing term added to drive Alfvén waves with coronal amplitudes between 5–30 km s^{-1}. We show that high-frequency waves can generate heating corresponding to a $\sim$10 per cent increase of the initial coronal shell temperature, chromospheric upflows of up to 0.6 km s^{-1} and a coronal shell mass increase of $\sim$15 per cent. These changes are sufficient to alter and maintain a new coronal loop density structure, broadening the region where efficient phase mixing (and therefore heating) occurs. In contrast, low-frequency waves are unable to be effectively dissipated, resulting in minimal changes to the loop structure. We see little evidence of wave energy accumulation in the corona and are unable to conclude that the dissipation of low-frequency Alfvén waves can be an effective heating mechanism in coronal loops in the setup used in this study.

Key words: (magnetohydrodynamics) MHD – Sun: atmosphere – Sun: corona – Sun: oscillations – methods: numerical.

1 INTRODUCTION

The coronal heating problem is a longstanding question, with the heating by magnetohydrodynamic (MHD) wave energy one suggested mechanism to address the problem (see reviews by e.g. Parnell & De Moortel 2012; Arregui 2015; Klimchuk 2015; Van Doorsselaere et al. 2020; Srivastava et al. 2021). Observational data indicates that a wide spectrum of MHD waves is present in the corona, carrying a significant amount of wave energy (e.g. De Moortel & Nakariakov 2012; Jess et al. 2016; Hinode Review Team et al. 2019). The presence of waves does not necessarily imply that the energy contained in these waves is dissipated on time and/or length-scales that address the coronal heating problem (see e.g. Arregui 2015). However, Okamoto et al. (2015) presented direct observational evidence of the dissipation process of MHD waves and subsequent heating, supported by numerical simulations in an accompanying paper by Antolin et al. (2015).

Classical dissipation of wave energy has long been known to be too inefficient in coronal plasma due to the large associated length-scales, with phase mixing suggested as one mechanism to address this problem (Heyvaerts & Priest 1983). Phase mixing occurs

when Alfvén waves propagate along neighbouring field lines with different Alfvén speeds, becoming increasingly out of phase, creating smaller length-scales which increase the efficiency of dissipation. Heyvaerts & Priest (1983) also postulated that the efficiency of wave energy dissipation can be enhanced if waves become trapped and phase mix in time. Such conditions can occur in coronal loops, where for example reflection off the transition regions (TR) could effectively trap low-frequency waves in the corona, allowing for the build up of wave energy over time and creating the conditions for temporal phase mixing. In contrast, the dissipation of phase mixed high frequency waves is known to be highly efficient, but the energy of these waves is more easily lost through transmission through the TRs downwards into the chromosphere (see e.g. Hollweg 1984; Berghmans & de Bruyne 1995; De Pontieu, Martens & Hudson 2001). Hence, it is still unclear whether the dissipation of high or low-frequency waves is more likely to contribute effectively to coronal heating.

When impulse heating events occur in the corona, the increased conductive flux drives material from the chromosphere upwards into the corona through evaporation, increasing coronal density. Unless the heating is maintained, the enhanced radiation and thermal conduction cool the corona, draining mass from the loop. Observational evidence of chromospheric upflows and downflows has been found in multiple studies (e.g. Winebarger et al. 2013), and 3D modelling

★ E-mail: hac22@st-andrews.ac.uk

has suggested that chromospheric flows and waves may result from the same impulsive events (Ofman, Wang & Davila 2012).

Computational modelling of Alfvén wave phase mixing is challenging as high resolution is required to fully resolve the small length-scales of the phase mixed waves. The complex physics of the chromosphere presents additional computational challenges and therefore is often neglected, but recent work by McMurdo et al. (2023) studied the phase mixing of Alfvén waves in a partially ionized plasma. For high frequency waves, they showed that depending on the ionization degree of the plasma, Cowling diffusion may be sufficiently large to balance radiative losses of the chromosphere. For our study, where our main focus is on the coronal aspects of the model, we simplify the latter problem by considering the chromosphere as a simple isothermal mass reservoir at both ends of the loop (e.g Cargill, Warren & Bradshaw 2015). The importance of numerical resolution in the TR has been a point of considerable study, with Bradshaw & Cargill (2013) finding that an underresolved loop TR can underestimate the peak density by at least a factor of two. To address this problem whilst avoiding unworkable computational costs, Lionello, Linker & Mikić (2009) and Mikić et al. (2013) proposed modifying the thermal conductivity and optically thin radiation below a fixed temperature value, leading to a broadening of the TR without significantly changing the coronal properties of the loop. An alternative method was developed by Johnston et al. (2017) who treated the TR as a discontinuity, conserving energy through the implementation of a jump condition. This approach has been expanded into the Transition Region Adaptive Conduction (TRAC) method, which removes the influence of numerical resolution on the coronal density response to heating (see e.g Johnston & Bradshaw 2019; Johnston et al. 2021; Zhou et al. 2021, for examples of TRAC implementation).

Most computational models used to study phase mixing in coronal loops start from a pre-existing Alfvén speed profile, often by imposing a gradient in the density and temperature to maintain pressure balance. Cargill, De Moortel & Kiddie (2016) investigated the self-consistency of such models, showing that phase mixing can increase the efficiency of wave energy dissipation, but that the heating was not sufficient to maintain any imposed density gradients required to phase mix. They also analysed whether the chromospheric evaporation generated by heating would be sufficient to modify the local density profiles, concluding that the density remained largely unmodified within the cooling and draining time-scales (see also Ofman, Klimchuk & Davila 1998). Van Damme et al. (2020) self-consistently explored the feedback process through evaporation associated with Alfvén wave phase mixing, using an imposed background heating profile to create a loop profile with shell (boundary) regions with strong Alfvén speed gradients. Although the high frequency waves were efficiently dissipated, only modest heating occurred inside the shell regions, which did not generate a sufficient mass increase through evaporation to affect the local density profile. Furthermore, the background heating profile was multiple orders of magnitude larger than the wave heating, signifying that wave heating alone may be unable to maintain the density structure required for phase mixing.

Observational studies have mostly shown coronal wave oscillations with periods of a few minutes (e.g. De Moortel & Nakariakov 2012), which in this paper we will consider to be low-frequency waves. Low-frequency waves are of particular interest to the coronal heating question as they are thought to be efficient carriers of energy. In addition, if some of the wave energy carried by the low-frequency waves can reach the corona, the steep TRs at both ends of a coronal loop may act as a barrier, effectively trapping the wave energy in the

coronal part of the loop. *In situ* generation would be an alternative possibility to lead to low-frequency wave energy in the coronal part of the loop. Although phase mixing would be slower (and would possibly be temporal rather than spatial phase mixing), if the wave energy is largely trapped in the coronal part, it would still lead to efficient dissipation.

In this paper, we expand upon the model used in Van Damme et al. (2020), increasing the amplitude of the coronal waves to match amplitudes suggested by observational data and extending the study to lower frequency waves. A 2D coronal loop model is presented, containing a transverse density profile and continuous Alfvén wave driver. We investigate the heating generated from the viscous dissipation of phase mixed Alfvén waves, subsequent field-aligned flows, evolution of the density profile, and impact on the phase mixing process. The results are presented in three sections. First, a comparison between a viscous and ideal high frequency (period, $P = 10$ s) driver is performed. Second, a parameter study on the period of the high frequency driver, to examine the sensitivity of the system. Third, a comparison between the high frequency driver examined in part one and a low-frequency driver ($P = 100$ s) is presented.

2 METHOD

2.1 Model

To study the phase mixing of Alfvén waves, a 2D numerical model of a coronal loop is created using the LARE2D code (Arber et al. 2001). We solve the set of normalized MHD equations:

$$\frac{\partial \rho}{\partial t} + \nabla \cdot (\rho \boldsymbol{v}) = 0, \tag{1}$$

$$\rho \frac{D\boldsymbol{v}}{Dt} = -\nabla P - \rho \boldsymbol{g} + \boldsymbol{j} \times \boldsymbol{B} + \boldsymbol{F}_{\text{visc}} \tag{2}$$

$$\frac{\partial \boldsymbol{B}}{\partial t} = \nabla \times (\boldsymbol{v} \times \boldsymbol{B}) + \eta \nabla^2 \boldsymbol{B} \tag{3}$$

$$P = 2n k_{\text{B}} T \tag{4}$$

$$\boldsymbol{j} = \nabla \times \boldsymbol{B} \tag{5}$$

$$\rho \frac{D\epsilon}{Dt} = -P(\nabla \cdot \boldsymbol{v}) - \nabla \cdot \boldsymbol{q} + H_{\text{bg}}(x) - \rho^2 \Lambda(T) + Q_{\text{visc}}. \tag{6}$$

Here, ρ is the mass density, $\boldsymbol{v}$ is the velocity, D/Dt is the convective derivative, P is the gas pressure, $\boldsymbol{j}$ is the current density, $\boldsymbol{B}$ is the magnetic field, n is the number density, and $\epsilon = \frac{P}{\rho(\gamma-1)}$ the specific internal energy. The viscous force is given by: $\boldsymbol{F}_{\text{visc}} = \rho \nu \nabla^2 \boldsymbol{v}$, where $\mu = \rho \nu$ is the dynamic viscosity coefficient and $Q_{\text{visc}} = \rho \nu \nabla \boldsymbol{v} : \nabla \boldsymbol{v}^T$ is the corresponding heating term. A semicircular field-aligned gravitational acceleration $g_{\parallel}(y) = g_{\odot} \cos\left(\frac{\pi y}{2y_{apex}}\right)$ is included. The conductive flux is given by $\boldsymbol{q} = -\kappa \frac{(\boldsymbol{B} \cdot \nabla T)\boldsymbol{B}}{B^2}$ and the optically thin radiative loss function $\Lambda(T) = \chi T^{\alpha}$ (Klimchuk, Patsourakos & Cargill 2008).

To obtain a 2D coronal loop model, a 1D thermodynamic equilibrium in the field-aligned direction is combined with a transverse heating profile. The coordinate system used defines y as the field-aligned direction, x as the cross-field direction, and z as the invariant direction. The field-aligned equilibrium comprises an 8Mm isothermal ($T = 2.0 \times 10^4$ K) chromosphere at each end of the loop, with a TR separating the chromospheric and coronal parts of the domain. A simplistic chromosphere that does not contain optically thick radiation or other appropriate chromospheric physics is used
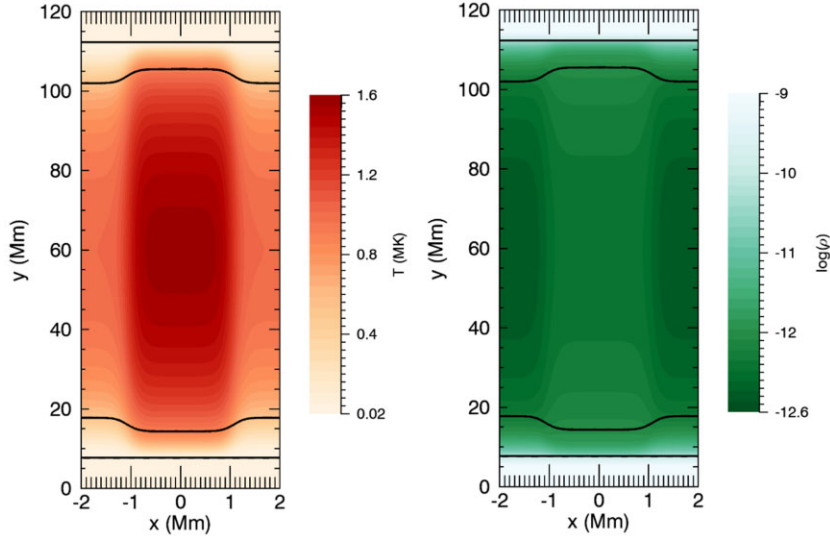
Figure 1. Contour plots of the initial temperature (left) and density (right) profiles after numerical relaxation. The horizontal black lines represent the TR boundaries.

as an isothermal mass reservoir (Cargill et al. 2015). The transverse background heating profile is given by

$$H_{\mathrm{bg}}(x) = \frac{H_2 + H_1}{2} + \frac{H_2 - H_1}{2} \tanh a(-|x| + b), \qquad (7)$$

where $a = 5\,\mathrm{Mm}^{-1}$ and $b = 1\,\mathrm{Mm}$ are parameters that determine the steepness and width of the heating function respectively, and $H_2 = 4H_1$ and $H_1 = 3.6 \times 10^{-6}\,\mathrm{J\,m^{-3}\,s^{-1}}$ are the background heating parameters used to obtain the 1D thermodynamic equilibrium in the interior.

Periodic boundary conditions are implemented in the x-direction and zero gradient boundary conditions are applied in y. The numerical domain is $4\,\mathrm{Mm} \times 120\,\mathrm{Mm}$, with a grid resolution of 256×4096. A temperature floor is set at $T = 2.0 \times 10^4\,\mathrm{K}$. We adopt the widely used approach of Lionello et al. (2009) and Mikić et al. (2013) to model a broader TR in order to improve the spatial resolution of the TR with this grid:

$$\kappa_\parallel(T) = \begin{cases} \kappa_0 T^{\frac{5}{2}} & T \geq T_{\mathrm{c}} \\ \kappa_0 T_{\mathrm{c}}^{\frac{5}{2}} & T < T_{\mathrm{c}} \end{cases} \qquad (8)$$

$$\Lambda(T) = \begin{cases} \Lambda(T) & T \geq T_{\mathrm{c}} \\ \Lambda(T) \left(\frac{T}{T_{\mathrm{c}}}\right)^{\frac{5}{2}} & T < T_{\mathrm{c}}. \end{cases} \qquad (9)$$

By increasing the thermal conduction and decreasing the optically thin radiation below a cutoff temperature T_{c}, the temperature lengthscale $L_{\mathrm{T}} = T/|\frac{\partial t}{\partial y}|$ is increased to above the size of the grid resolution, numerically resolving the TR. For all simulations presented, T_{c} is set to $5.0 \times 10^5\,\mathrm{K}$.

Using an initially uniform magnetic field $B_y = 10\,\mathrm{G}$, the system is numerically relaxed until the field-aligned and cross-field velocities v_x and v_y are sufficiently small. After numerical relaxation, the cross-field heating profile creates a density ratio between the interior and exterior of $\rho_{\mathrm{i}}/\rho_{\mathrm{e}} = 2.5$ at the loop apex. Between the interior and exterior regions, there is a density gradient present where phase mixing can occur (see Fig. 1). We will refer to these regions as the 'shell' regions. The internal and external coronal domains are 90 Mm and 84 Mm in length, respectively.

2.2 Driver

A sinusoidal driver is applied to 10 gridpoints centred around y=10 Mm (i.e. inside the 1st TR) and uniformly across the x domain. The driver is implemented as an additional force in the z-component of the momentum equation:

$$F_z = -\rho V_0 \omega \cos(\omega t), \qquad (10)$$

where $\omega = \frac{2\pi}{P}$ is the angular frequency, P is the period of the driver and $V_0 = 24.5\,\mathrm{km\,s^{-1}}$ is a constant based on the local Alfvén speed. This additional force term generates Alfvén waves in the field-aligned direction, which propagate upwards into the corona and downwards into the chromosphere. The downwards waves will at some point reflect back upwards towards the corona, due to the large density gradients in the chromosphere. The location of reflection will differ depending on the numerical resolution, location of the driven region, and period of the driven waves.

For the high frequency cases presented in this paper, the chromospheric reflection will interact with the driven region after 700–900 s, whereas for the low-frequency simulations, the interactions occur after 2400 s. This is shown in Fig. 2, where the 10 s driver steps once after 700 s before oscillating around a constant value, and the 100 s driver steps every 2400 s. After reflections, both the 10 s and 100 s drivers generate Alfvén waves with coronal amplitudes of 5–30 km s^{-1}, which is consistent with observational values (e.g. McIntosh et al. 2011; Weberg, Morton & McLaughlin 2018).

3 RESULTS

The results of this paper are split into three sections. First, a detailed analysis is presented of a single simulation with a high-frequency driver (period P=10 s). Next, a parameter study of high-frequency drivers (P=10 - 12.5 s) is performed, to investigate the sensitivity of the system. Finally, the study is expanded to lower frequency drivers, with periods of P= 100, 300, 600 s and compared to a 10 s driver. For all non-ideal simulations, we use a dynamic viscosity $\rho\nu = 5 \times 10^{-4}\,\mathrm{kg\,m^{-1}\,s^{-1}}$, with zero resistivity to avoid diffusion of the background magnetic field. To distinguish between evaporative
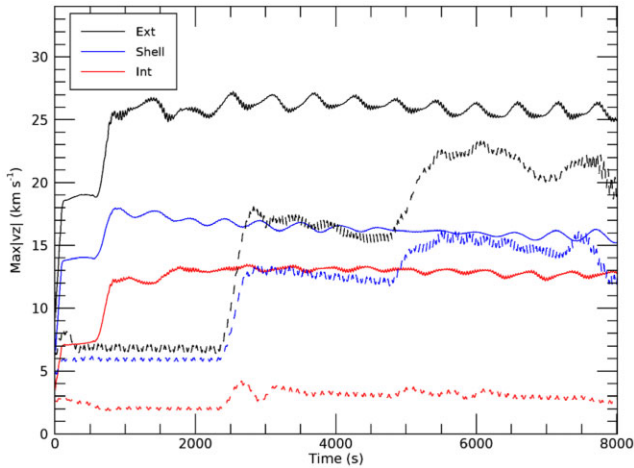
Figure 2. Plot of the maximum $|v_z|$ in the exterior (black), shell (blue), and interior (red) regions for the viscous $P = 10$ s (solid) and $P = 100$ s (dashed) simulations.
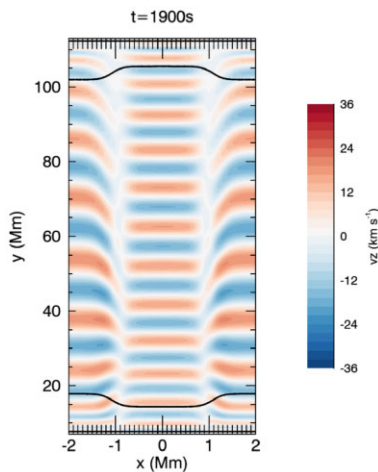
**Figure 3.** Contour plot of v_z at t=1900 s for the viscous P=10 s simulation.

upflows resulting from coronal heating and other field-aligned flows, ideal versions of the P=10 s and P=100 s drivers were also run.

3.1 $P = 10$ s simulations

Initially, we consider the case of a high frequency driver, generating Alfvén waves with a period of $P = 10$ s. For the 10 s driver, the chromospheric reflection interacts with the driven region at 700 s, after which the amplitude of the waves propagating into the corona remains roughly constant. The amplitude of the coronal Alfvén waves increases to between $12\text{--}27$ km s^{-1} (solid lines in Fig. 2), with the highest amplitudes occurring in the less dense external region.

Fig. 3 shows a contour plot of v_z for the P=10 s simulation at a time after the amplitude has increased. In the shell regions, efficient phase mixing creates fine scale structuring, leading to full dissipation of the waves. The wavelength of the waves in the corona is sufficiently small such that the TR does not act as a barrier, allowing almost all of the Alfvén waves in the interior and exterior regions to be transmitted out of the corona.

Fig. 4 shows the field-aligned component of the Poynting flux passing through the 1st (solid line) and 2nd (dashed line) TR-coronal boundaries, volume and time integrated inside the left shell region,
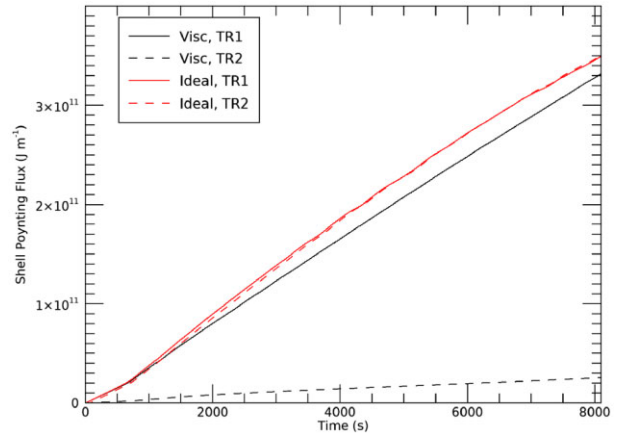

Figure 4. Plot of the time integrated Poynting flux, $\int_0^t \int_S [E \times B]_y \, dS \, dt$, where S is the TR-coronal boundary inside the left shell region. The solid lines represent the Poynting flux passing through the 1st TR-coronal boundary (black viscous, red ideal), and the dashed lines the 2nd TR-coronal boundary.

$\int_0^t \int_S [E \times B]_y \, dS \, dt$. The rate of flux injection (gradient of the solid line) changes once at the reflection time, before remaining constant, implying that a near constant amount of flux is injected into the system by the driver. As expected, the flux passing into and out of the coronal domain for the ideal simulation (red) is approximately equal. In the viscous simulation, nearly all the flux (93 per cent) is dissipated across the full width of shell region, indicating that even at the edges of the shell where the Alfvén speed gradient is weaker, phase mixing is still sufficiently efficient to dissipate the majority of the flux.

Viscous dissipation of the flux in the shell regions causes significant heating, generating evaporative upflows into the corona and hence increasing the coronal mass. Fig. 5 shows the relative change in temperature ($\frac{T - T_0}{T_0}$ – top row) and density (bottom row), and the field-aligned flow (v_y – middle row) in the first half of the loop, at five different times in the simulation. From the temperature at early times (first 2 panels), it is clear that the initial heating occurs inside the coronal region, with the temperature change travelling downwards into the TR at later times ($t = 1000$ s panel). The top and bottom panel of Fig. 6 display the evolution of temperature and density at the apex of the loop in the centre of the left shell region ($x = -1.1$ Mm, $y = 60$ Mm). Limited heating occurs until the reflection time (first vertical dashed line in Fig. 6), after which the larger Poynting flux brings more wave energy into the corona, leading to stronger heating and the subsequent chromospheric evaporation begins to increase coronal density.

After 1900 s, there is a narrow band of heating at the centre of the shell regions, strong enough to generate evaporative upflows from the chromosphere. These upflows are visible in the middle panel at $t = 1900$ s in Fig. 5, with a positive v_y in the first half of the loop correlating to upflows from the 1st chromosphere into the corona. Panel 2 of Fig. 6 shows the field-aligned velocity, averaged over the 1st TR-coronal boundary in the left-hand shell region as a function of time for both the viscous (black line) and ideal (red) simulations. Field-aligned flows such as slow waves and ponderomotive upflows are present in both simulations whereas evaporative upflows will only be present in the viscous simulation as a result of the heating. The difference between the black (viscous) and red (ideal) lines is a lower bound for the size of the evaporative upflows, as any flow in the non-ideal simulation will be damped by the viscosity. After the coronal v_z increases at 700 s, evaporative upflows of up to 0.6 km s^{-1}
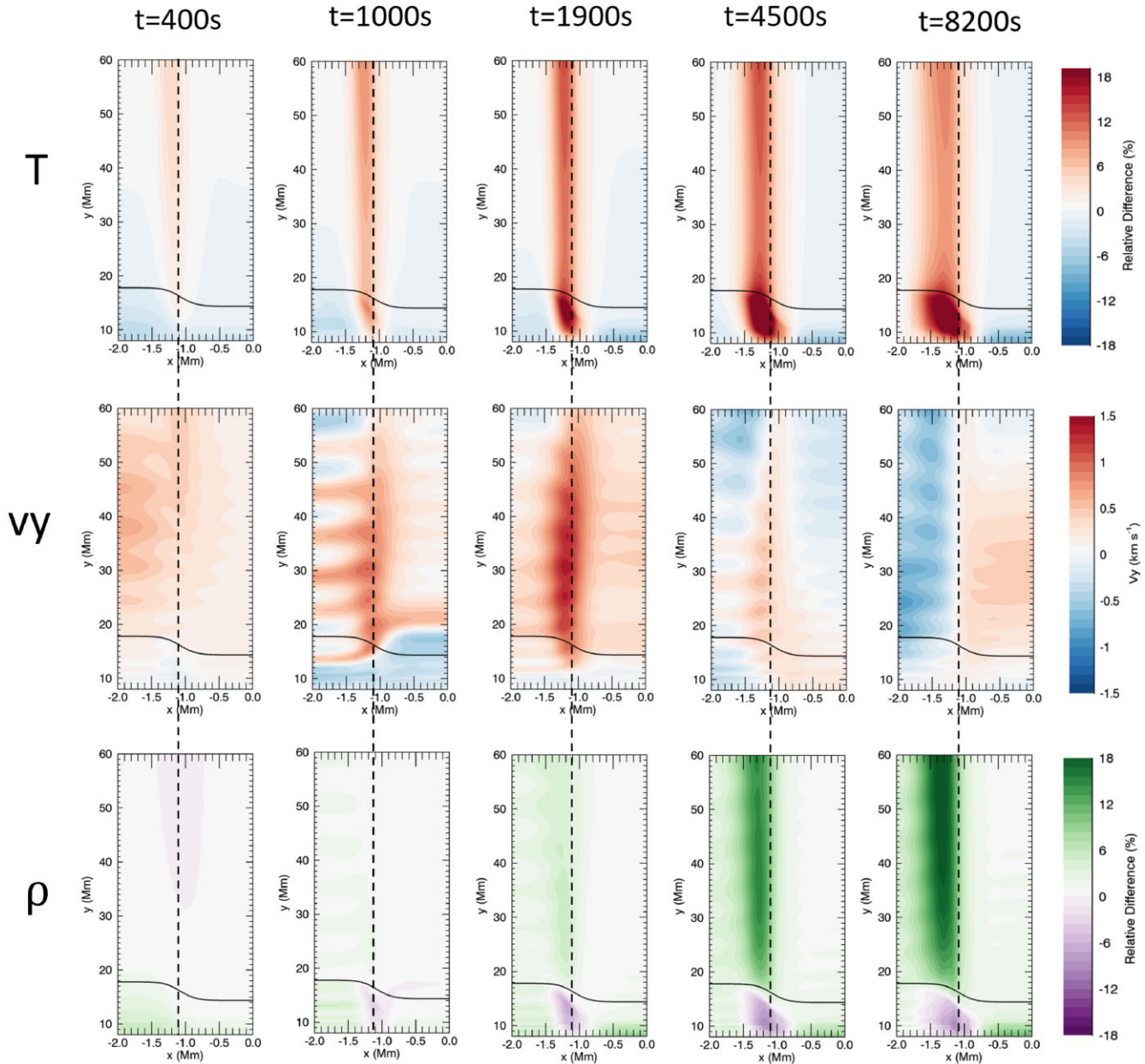
Figure 5. Contour plots of $(T - T_0)/T_0$ (top), v_y (middle) and $(\rho - \rho_0)/\rho_0$ (bottom) for the P=10 s viscous simulation at 5 different times. A quarter of the TR-coronal domain is presented ($-2\,\text{Mm} < x < 0\,\text{Mm}$, $8\,\text{Mm} < y < 60\,\text{Mm}$). The horizontal black line represents the TR-coronal boundary, and the dashed line corresponds to the centre of the shell region ($x = -1.1\,\text{Mm}$, same value as taken in the upper and lower panels of Fig. 6).

occur at the 1st TR-boundary (second dashed line in Fig. 6), with similarly sized flows also occurring at the 2nd TR-boundary. At this early stage of the simulation, only a small amount of plasma has been moved into the corona, thus the coronal density increase shown in the first three panels of Fig. 5 is modest.

After 4500 s, the heating in the shell region has resulted in a coronal temperature increase of 15 per cent and the width of the heated region has broadened outwards towards the exterior of the domain. Partly, this is due to the weaker density gradients, phase mixing and dissipation in this region, generating a less efficient and therefore slower heating mechanism towards the exterior. The temperature change enhances evaporative upflows, generating a density change and altering the phase mixing profile. In regions of initially weak dissipation, this accelerates the heating mechanism. This evolution

in time of the cross-field Alfvén gradient is shown in Fig. 7, where the gradients in the exterior significantly increase as the simulation evolves. By 4000 s, the shell region has expanded almost to the edge of the domain, with enhanced heating, upflows and coronal mass increase visible in the 4500 s column of Fig. 5. Thus, the initial heating generated by the driver causes sufficient thermodynamic feedback to broaden the initial transverse density profile, in such a way that the phase mixing process is enhanced. These increases only occur towards the exterior due to the larger amplitude and higher frequency waves providing more energy compared to the interior region, as well as the lower radiation (density) levels. A decrease in the size of the Alfvén gradients also occurs as the simulation evolves, from an initial $\frac{\mathrm{d}V_A}{\mathrm{d}x} = \pm 1.5\,\text{s}^{-1}$ to $\frac{\mathrm{d}V_A}{\mathrm{d}x} = \pm 1.1\,\text{s}^{-1}$ (Fig. 7). This is due to the enhanced coronal density from the evaporative upflows,
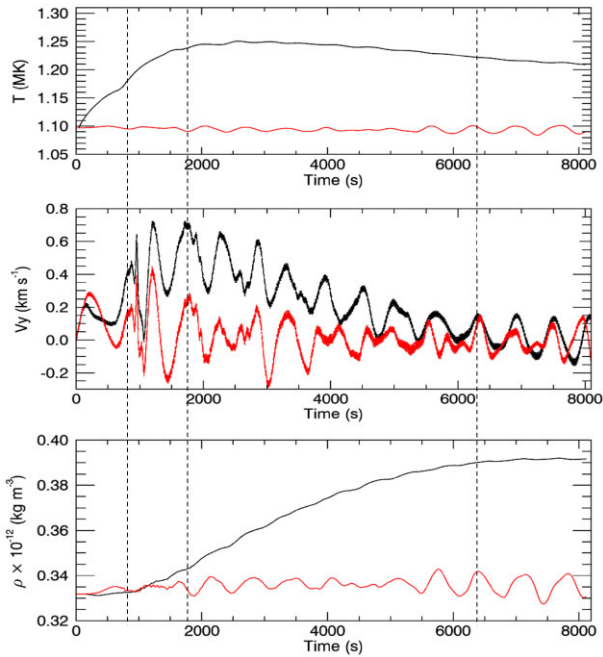
Figure 6. Top: evolution of the temperature at the apex of the loop in the centre of the shell region (dashed line in Fig. 5) for the $P = 10$ s viscous (VD – black) and ideal (ID – red) simulations. Middle: v_y, integrated over the 1st TR-coronal boundary in the left-hand shell region as a function of time. Bottom: repeat of top panel but for the density.
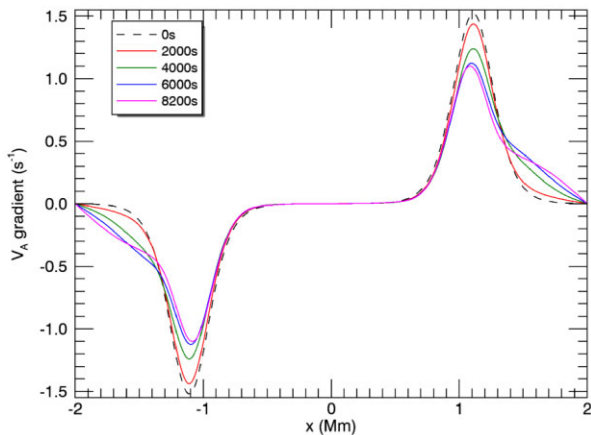
Figure 7. Plot of the evolution of the cross-field derivative of the Alfvén speed profile at the loop apex ($y = 60$ Mm), at different times in the P=10 s simulation.

reducing the difference in density between the shell and interior regions. Despite this decrease in the efficiency of the phase mixing, it remains sufficient to completely dissipate the Poynting flux by the loop apex at all times in the simulation.

Evaporative upflows steadily decrease in size after 1900 s, as the heating at the centre of the shell becomes weaker and the corona becomes saturated with mass from the chromosphere. After 6400 s (third dashed line in Fig. 6), flows in the ideal and viscous simulations become indistinguishable, with the coronal density maintained at 18 per cent higher than the initial value in the viscous case. At the end of the simulation (8200 s), the coronal temperature at the apex in the shell region has increased to 1.2 MK (Fig. 6), although this is less than the maximum temperature of 1.25 MK reached at 2500 s. This
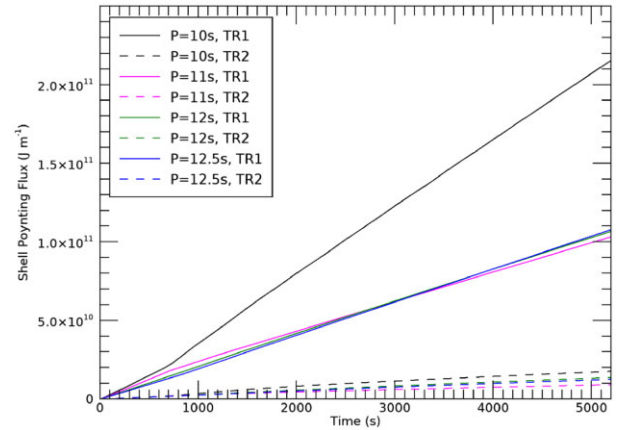

Figure 8. Plot of the time integrated Poynting flux, $\int_0^t \int_S [E \times B]_y \, dS \, dt$, for the P=10 s (black), P=11 s (pink), P=12 s (green), and P=12.5 s (blue) simulations. The solid lines represent the Poynting flux passing through the 1st TR-coronal boundary and the dashed lines the 2nd TR-coronal boundary.

is due to the lag time between heating and coronal mass increase, thus as the density continues to increase until 6400 s the radiation also increases until this time. The driver is unable to provide enough energy to support a coronal temperature of 1.25 MK, therefore the energetic losses of radiation and thermal conduction gradually cool the corona down to $\approx$1.2 MK. The system approaches a new steady state, where the driver continually provides energy to support a new hotter and denser corona against the increased energetic losses. The imposed transverse density profile has been permanently broadened by the heating process, enhancing regions of previously weak phase mixing.

3.2 High frequency period parameter study

The choice of a 10 s driver in Section 3.1 was an arbitrary choice. Driven simulations such as the ones presented in this paper are likely to be sensitive to variables such as the period of the driver, as the amplitude of the coronal waves is partially determined by the interactions between driven and reflected waves. Therefore, a parameter study was performed to explore how sensitive the system is to the period of the Alfvén driver in the high-frequency regime of our study. Three additional viscous high frequency driven simulations with periods of 11, 12, and 12.5 s were run for 5200 s and compared to the 10 s driver. Note that due to the ω factor in the coefficient of the momentum equation (equation 10), the amplitude of the Alfvén acceleration term will be different for the different frequencies.

Fig. 8 shows the time integrated Poynting flux passing through the TR1-corona (solid lines) and TR2-corona (dashed lines) boundaries at the centre of the shell region ($x = -1.1$ Mm). Initially, flux passing into the coronal domain at the TR1 boundary varies according to the period of the driver, with the smaller period drivers generating more flux due to the larger acceleration. However, after the interaction between the driven region and chromospheric reflected wave (occurring between 700–900 s), the 11 s driver begins to generate less flux than either the 12 s or 12.5 s drivers. This is due to the different interaction between the driven and chromospheric reflected waves, resulting in relatively lower amplitude waves travelling upwards into the corona in the 11 s case. In fact, the 11, 12, and 12.5 s drivers all inject less than half of the total flux of the 10 s driver after 5200 s. This is due to a combination of the smaller acceleration of the driver and the fact that the interaction between the driven and reflected waves generates
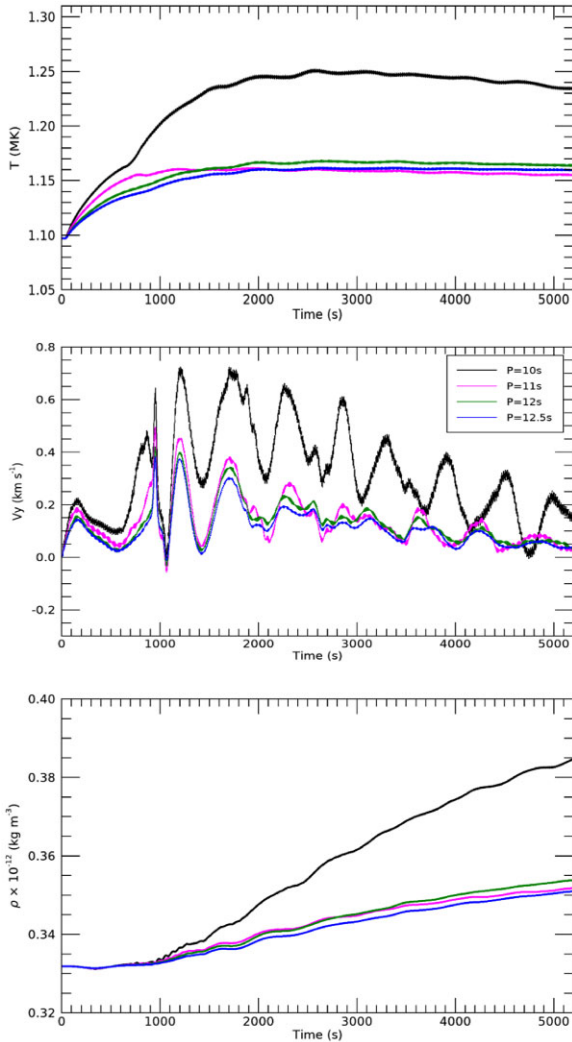
Figure 9. Top: evolution of the temperature at the apex of the loop in the centre of the shell region (dashed line in Fig. 5) for the P=10 s (black), P=11 s (pink), P=12 s (green), and P=12.5 s (blue) viscous simulations. Middle: v_y, integrated over the 1st TR-coronal boundary in the left-hand shell region as a function of time. Bottom: repeat of top panel but for the density.

the largest amplitudes for the 10 s driver. It is clear that the system is highly sensitive to the period of the driver. However, for all 4 periods, the Poynting flux at the TR2 boundary is substantially smaller than at TR1, indicating that phase mixing is efficient in dissipating the waves for these high-frequency wavelengths.

The different behaviour of the 10 s driver becomes further apparent when comparing shell temperature and density change at the loop apex to the other high frequency drivers (Fig. 9). The 11, 12, 12.5 s waves generate little additional heating, instead plateauing after an increase of only 0.05 MK in temperature. Only very modest upflows are generated (middle panel of Fig. 9) with little difference between the drivers. Note that the other v_y flows generated in the system will be larger for the smaller period drivers, due to a relatively larger force (acceleration) created by the driver. Evaporative upflows can only be estimated from the central panel of Fig. 9, however, it is clear that the 10 s simulation generates larger upflows. The change in density is similarly modest across the 11, 12, 12.5 s simulations, with only at most a 6 per cent increase in apex coronal density in the centre of the shell region.
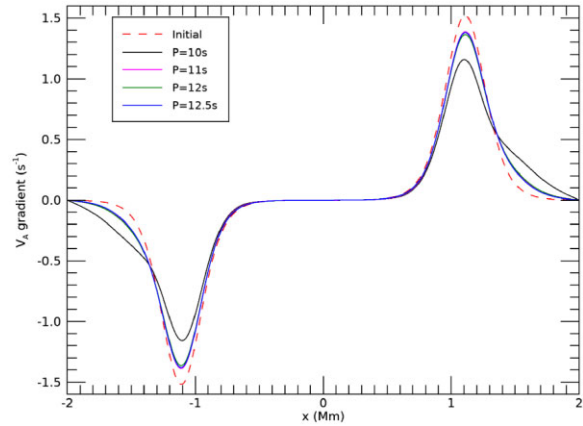
Figure 10. Plot of the cross-field derivative of the Alfvén speed profile after 5200 s for the high frequency simulations. The cross-section is taken at the loop apex ($y = 60$ Mm) and the red dashed line represents the initial profile.

Finally, Fig. 10 shows the cross-field density gradients for the 4 high-frequency drivers after 5200 s, compared to the initial cross-field gradient. The 11, 12, 12.5 s simulations all generate a near-identical change in the gradient, with a limited broadening towards the exterior. For the 10 s simulation, a sufficient level of heating is generated such that the thermodynamic feedback is able to affect the transverse density profile and enhance the phase mixing process. However, the other high frequency drivers generate lower amplitude waves which are unable to heat the corona enough to alter the transverse density profile significantly. It is clear that the system is highly sensitive to the period of the driver, due to the complex interaction between the driven region and reflected wave determining the amplitude (and therefore energy) of the coronal Alfvén waves.

3.3 Low-frequency driver

Low-frequency Alfvén waves are of particular interest in the context of coronal heating. It has been suggested that low-frequency waves could become trapped inside the coronal domain as longer wavelengths are expected to be reflected by the strong density gradients present in the TR, hence allowing a build up of wave energy. Simulations of a driver with P=100, 300, 600 s were performed. To offset the decrease in the magnitude of the acceleration caused by the ω factor (equation 10), V_0 was increased by a factor of 5, 15, and 30 respectively, resulting in all of the low-frequencies drivers having the same magnitude of acceleration. The acceleration was not normalized to the same value as the P=10 s driver to avoid non-linearities in the chromosphere. For the 100 s simulation, only 1 full wavelength fits inside the coronal domain at any time, with between 1.2–1.4 λ in the corona. In the $P = 300, 600$ s cases, a full wavelength is never present in the coronal part of the loop. Note that in Heyvaerts & Priest (1983), the presence of several wavelengths is implied in their assumption of the strong phase mixing limit and weak damping approximation. Hence, spatial phase mixing is expected to be much less efficient in all low-frequency cases, as there are never multiple wavelengths present in the coronal domain.

As discussed in Section 2.2, the amplitude of the Alfvén wave will continually evolve for all of the low-frequency drivers. Fig. 2 shows that in the 100 s simulation steps in wave amplitude occur every 2400 s, with similar amplitude waves occurring in the shell region in the 10 and 100 s cases after 4800 s. Before the interaction between the driver and the waves reflected at the chromosphere,
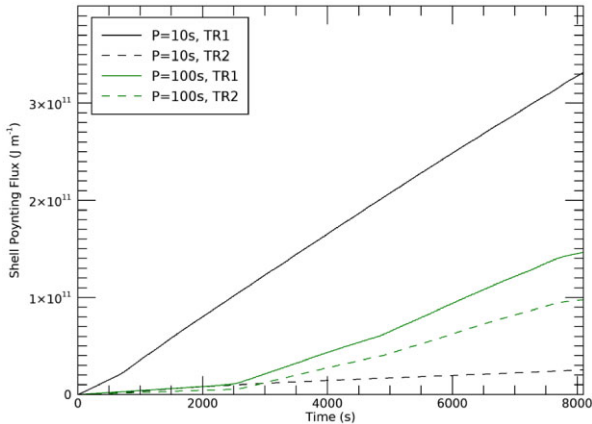
Figure 11. Plot of the time integrated Poynting flux, $\int_0^t \int_S [E \times B]_y \, dS \, dt$, for the P=10 s (black) and P=100 s (green) simulations. The solid lines represent the Poynting flux passing through the 1st TR-coronal boundary and the dashed lines the 2nd TR-coronal boundary.

the injected shell Poynting flux is substantially smaller in the 100 s simulation than in the 10 s simulation. This is partially due to the initial acceleration of the driver being half the size, which would result in a four-fold difference (Poynting flux, $[PF]_y \cong B_y B_z v_z$). However the initial gradient of the 100 s shell Poynting flux is less than one fourth of the 10 s, indicating that the low-frequency driver is less able to transmit flux into the corona as the steep TR allows less transmission of the longer wavelength waves. The injection rate of the Poynting flux of the 100 s driver increases after the first and second reflection, but always remains below the rate of the 10 s driver. The dissipation rate (difference between solid and dashed lines in Fig. 11) is significantly lower in the 100 s simulation with only one third of the flux being dissipated, confirming that phase mixing is indeed much less efficient in comparison to the high-frequency simulations.

The combination of less flux injected and a less efficient dissipation mechanism results in significantly less heating. After 8200 s, the 100 s driver has generated only a modest amount of heating, an order of magnitude smaller than the 10 s driver. Moreover, Fig. 12 shows that the region of temperature increase is restricted to only the very centre of the shell regions, i.e. the region where the strongest phase mixing occurs. The coronal density increase is also an order of magnitude smaller and similarly is restricted to the centre of the shell. Due to this restriction and the modest heating, there is no change to the initial transverse density gradient. The upflows generated by the 100 s driver are too small to distinguish from the other field-aligned flows (Fig. 13, middle panel).

To understand the efficiency of energy conversion, we consider the cumulative increase in coronal shell internal energy (solid lines in Fig. 14) and the instantaneous coronal shell wave energy (dashed lines). Initially, the 10 s case generates three times more wave energy, but after two reflections have occurred in the 100 s simulation, both simulations generate a comparable amount of wave energy. The 10 s case experiences a rapid increase in internal energy, before plateauing after 4000 s. This corresponds to when the temperature in the centre of the shell is no longer increasing (and begins to cool due to radiation continually increasing as the density increases), with some heating still occurring towards the exterior. The total internal energy of the system is maintained by the continual efficient dissipation of the wave energy. In comparison, the rate of internal energy increase in the 100 s simulation is much more gradual, and it takes about

4800 s before the available wave energy is similar between the two simulations. The system heats much slower due to the relatively inefficient conversion of wave energy to heating and the internal energy of the system continues to increase for the whole 8200 s duration of the simulation. The instantaneous wave energy of the 100 s case remains near constant in between the 2400 s reflection times, implying that there is no build of energy inside the coronal domain.

Fig. 14 also shows results for simulations with a 300 and 600 s driver, with V_0 normalized so that all of the low-frequency drivers have the same acceleration (equation 10). The wavelengths associated with these periods are larger than the coronal domain, therefore the driver cannot establish a resonant wave. Due to this, the coronal amplitude of the Alfvén waves generated for the 300 and 600 s cases are always small (less than 4 km s^{-1}) and the associated wave energy is an order of magnitude smaller than the 100 s case. The larger wavelengths should be associated with more trapping of wave energy in the corona, however similar to the 100 s case, the wave energy remains approximately constant between reflection times. We are unable to find evidence that wave trapping leads to a noticeable build of wave energy inside the coronal domain, therefore the conditions required for phase mixing in time do not occur for any of the low-frequency cases. As such, the dissipation mechanism is limited to only spatial phase mixing, which is not sufficiently efficient to dissipate the low-frequency wave fully in this setup. Thus, all low-frequency waves tested result in insignificant heating and density changes, with no notable evolution of the Alfvén speed profile.

4 DISCUSSION AND CONCLUSIONS

In this paper, a 2.5D atmospheric model of a coronal loop is presented, containing an isothermal chromosphere (acting as a mass reservoir) and an artificially broadened TR (following the method proposed by Lionello et al. 2009; Mikić et al. 2013). A cross-field heating profile is imposed to establish a transverse density profile, creating a shell region where phase mixing can occur. An Alfvén wave driver is applied to the system as an additional forcing term in the momentum equation, which through the interaction of driven and reflected waves generates coronal Alfvén waves at the upper end of observed amplitudes for either high or low-frequency waves (Fig. 2).

The simulations presented in this study showed that spatial phase mixing of the high frequency waves is efficient, with effective dissipation occurring even in regions with a relatively weak Alfvén speed gradient. Heating of up to 0.15 MK occurs inside the shell region, and the heated region broadens to beyond the initial shell region. Through comparison of an ideal and viscous simulation, chromospheric evaporative upflows are isolated from other field-aligned flows and estimated to be of the order of 0.5 km s^{-1}. These upflows are sufficient to deform the imposed transverse Alfvén speed gradient, reducing the size of gradients at the centre of the shell. Notably, the profile also broadens outwards to the exterior of the loop, enhancing weak phase mixing at the edge of the imposed shell region. These results imply that the thermodynamic feedback of the heating can affect the Alfvén speed profile, sometimes reducing phase mixing and at other times expanding the region where phase mixing can occur.

The 10 s driver was able to establish and maintain a new, hotter coronal equilibrium, where efficient dissipation of the wave energy balanced the increased energetic losses from radiation and thermal conduction. The mass increase was also maintained, remaining over 15 per cent higher 6000 s after the temperature increase, and after all
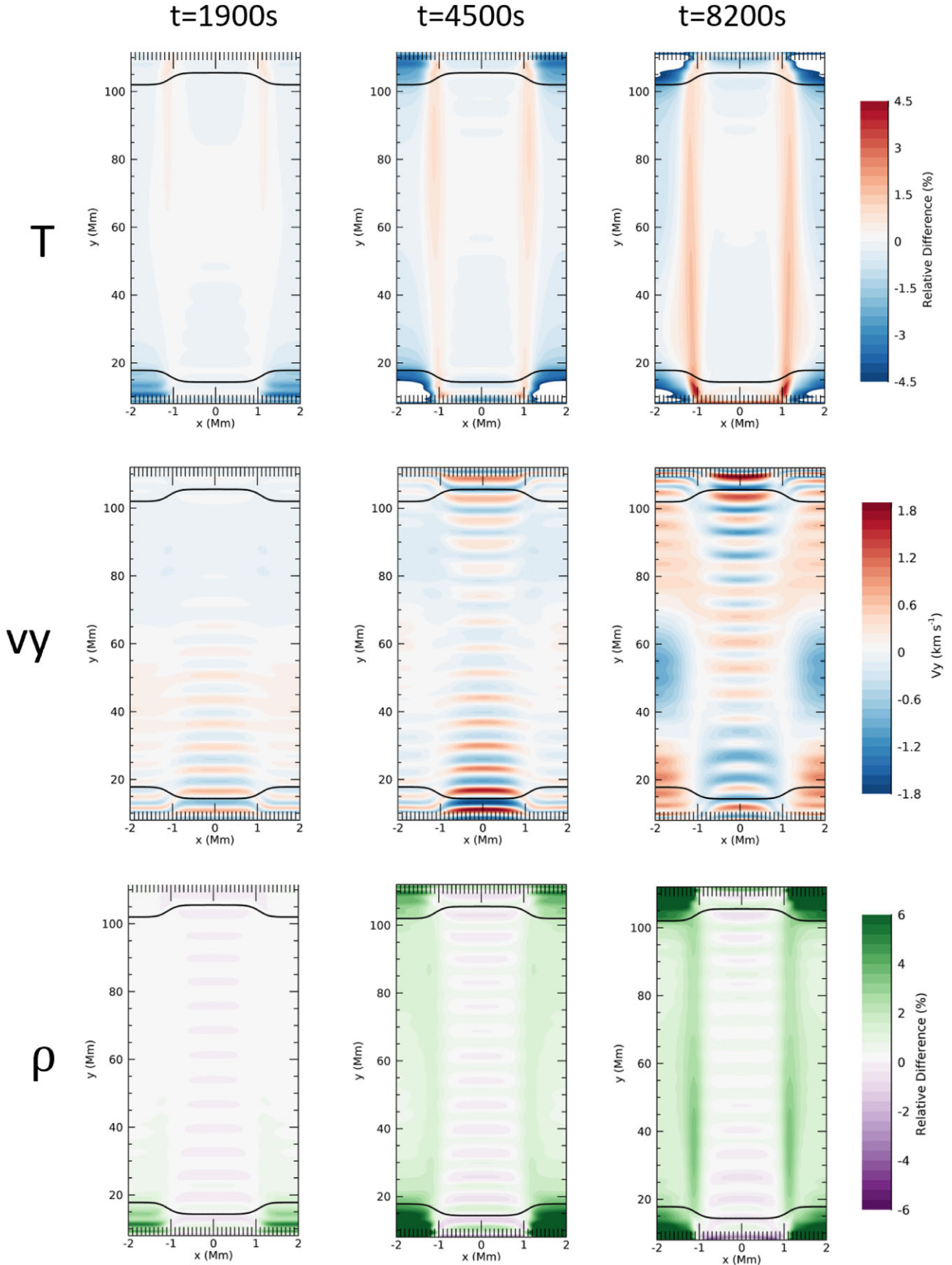
Figure 12. Contour plots of $(T - T_0)/T_0$ (top), v_y (middle), and $(\rho - \rho_0)/\rho_0$ (bottom) for the P=100 s viscous simulation at 3 different times. The full TR-coronal domain is presented ($-2\,\mathrm{Mm} < x < 2\,\mathrm{Mm}$, $8\,\mathrm{Mm} < y < 112\,\mathrm{Mm}$), where the horizontal black lines represent the TR-coronal boundaries.
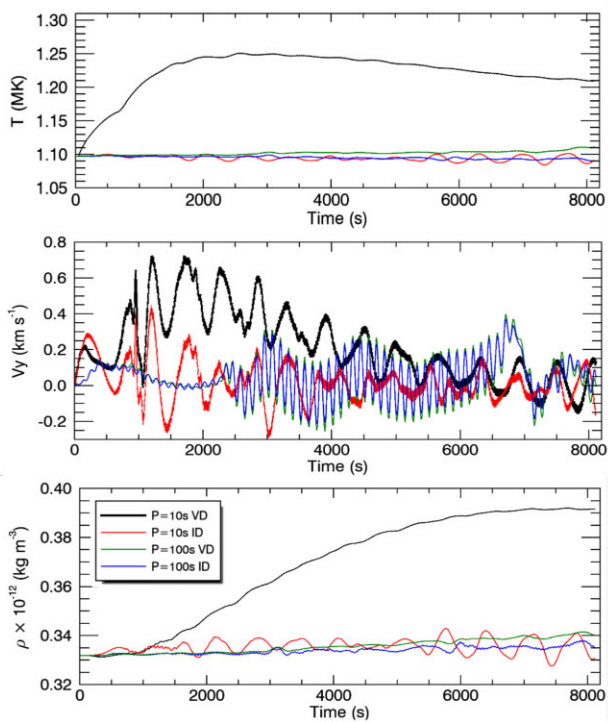
Figure 13. Top: evolution of the temperature at the apex of the loop in the centre of the shell region (dashed line in Fig. 5) for the P=10 s and P=100 s viscous (VD – black, green) and ideal (ID – red, blue) simulations. Middle: v_y, integrated over the 1st TR-coronal boundary in the left-hand shell region as a function of time. Bottom: repeat of top panel but for the density.
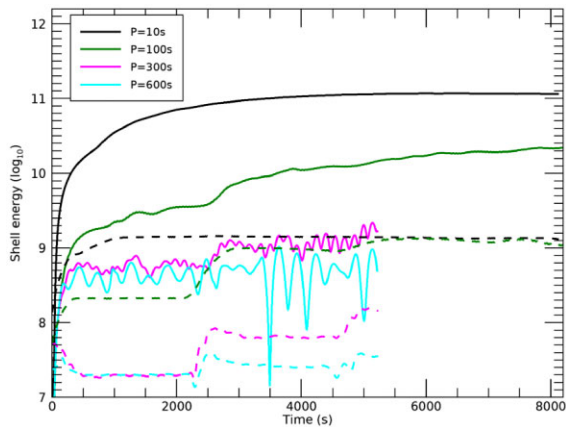
Figure 14. Plot of the change in internal energy in the left coronal shell (solid) for the P=10 s (black), P=100 s (green), P=300 s (pink), and P=600 s (teal) simulations, and instantaneous coronal wave energy ($\frac{1}{2}\rho v_z^2 + B_z^2/2\mu_0$) in the left shell (dashed). A smoothing factor is applied to the wave energy.

chromospheric upflows ceased. Effectively, the high frequency driver can be thought of as acting as a portion of a background heating to the new equilibrium, continually injecting energy into the corona. However, the viscous heating associated with the wave dissipation is less than 10 per cent of the total background heating function used to create the initial transverse density profile and is only efficient in the shell region of the loop where phase mixing occurs. Therefore the wave-based heating is not sufficient to maintain the imposed density structure, which agrees with conclusions previously found in other

wave heating studies (for example Cargill et al. 2016; Pagano, De Moortel & Morton 2020).

In Section 3.2, the high frequency results are shown to be highly sensitive to the period of the driver, even within the narrow period range of 10–12.5 s. Although the efficiency of the dissipation remains high for each of the high frequency periods used in this study, the amount of wave energy generated by the interaction between the driver and reflections changes significantly even for small changes in the period of the driver. However, it is important to note that there is nothing inherently special about the 10s driver. Larger coronal amplitudes are generated for this driver due to the highly constructive interaction between the reflected and driven wave. Only due to a combination of the chosen physical values and computational properties (e.g. loop length, chromospheric density gradient, position of the driver, and numerical resolution) is the 10 s driver the 'best case scenario' for our setup. In addition, our setup uses a monochromatic driver whereas the spectrum of waves in coronal loops is expected to have a broad-band nature (see e.g. Pagano & De Moortel 2019; Howson & Breu 2023; Howson & De Moortel 2023, for examples of broad-band drivers).

In contrast to the high frequency waves, the low-frequency waves do not phase mix efficiently, resulting in minimal heating and negligible upflows and density increase and, hence, no noticeable effect on the transverse Alfvén speed profile. For the 100 s driver, the temperature increased by only 0.01 MK after 8200 s, with upflows so weak that they were indistinguishable from the other field-aligned flows. After 4800 s, the interaction between driver and reflections generated coronal Alfvén waves of similar amplitude in the 10 and 100 s drivers, with a slightly larger shell coronal wave energy in the 100 s simulation (Fig. 14). Therefore the model does reach a stage where a high and low-frequency driver generate a similar amount of wave energy in the corona, but it is the efficiency of the dissipation that distinguishes the thermodynamic evolution of the two systems. This also indicates that conditions for efficient temporal phase mixing are not being created in the simulation, i.e. the waves are not being sufficiently trapped in the corona by the TRs. The Mikić approach we used in our simulations decreases the size of the density gradients in the TR and therefore the TR may act as less of a barrier to the coronal Alfvén waves. To establish the effect of the Mikić approach, an additional simulation for the $P = 100$ s driver was run with a lower critical temperature of $T_c = 2.5 \times 10^5$ K. For this value of the cutoff temperature, the impact of the Mikić approach on the TR density structure is limited. However, even in this case there was still no clear evidence of significant wave trapping occurring, and the overall behaviour was similar in all regards.

Moreover, even when the study was expanded to Alfvén waves with periods of 300 and 600 s, we observed no evidence of significant build-up of wave energy in the coronal domain (pink and teal lines in Fig. 14). Although it is possible that further increasing the period may lead to more energy trapping, the dissipation rate due to spatial phase mixing will consequentially decrease. Fig. 15 shows a ratio of the Poynting flux in the shell region passing through the first and second TR-coronal boundaries for the first 2300 s of all viscous simulations presented in this paper, (PF(TR1) − PF(TR2))/PF(TR1)). The high frequency cases are shown by the warm colours, with a ratio between 0.86–0.9, i.e a coronal dissipation rate between 86–90 per cent, indicating highly efficient phase mixing. In contrast, the dissipation rate drops below 50 per cent for all of the low-frequency cases, with a decrease in dissipation as the period increases from 100 to 600 s. As the wavelength increases, the cross-field Alfvén speed gradients decrease, reducing the ability of the system to create the fine-scale structuring required for dissipation.
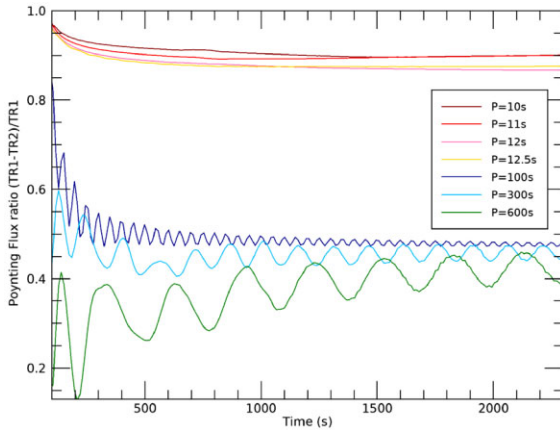
Figure 15. Evolution of the ratio of the Poynting flux in the shell region passing through TR1 and TR2 for all high and low-frequency simulations, $(PF(TR1) - PF(TR2))/PF(TR1)$. The different colours correspond to the different high-frequency ($P = 10$ s brown, $P = 11$ s red, $P = 12$ s pink, $P = 12.5$ s yellow) and low-frequency simulations ($P = 100$ s dark blue, $P = 300$ s light blue, $P = 600$ s green).

One important aspect of our study is the value of the viscosity we have used ($\rho\nu = 5 \times 10^{-4}$ kg m^{-1} s^{-1}). A similar value has been previously used for studies of coronal dynamics with the LARE code (see e.g. Howson et al. 2019; Van Damme et al. 2020; Reid, Threlfall & Hood 2023). Although this is about 6 orders of magnitude larger than the predicted coronal value for the perpendicular component of the viscosity given by classical plasma theory, the choice of a much larger value can be motivated as follows. Due to computational limitations, it is not possible to achieve the small length-scales representative of the solar corona, therefore a larger viscosity value is used to mimic the small-scale behaviour. In addition, other physical processes such as plasma turbulence are thought to significantly enhance viscous damping via the generation of small scales, as suggested in Ruderman & Petrukhin (2017).

To explore if the choice of the value of viscosity significantly altered the dissipation of low-frequency Alfvén waves, additional simulations with an increased viscosity were run for the 100 s case. As expected, increasing the viscosity by an order of magnitude increased the proportion of Poynting flux dissipated and the subsequent amount of heating. However the increases were limited and only in the centre of the shell did the rate of dissipation increase significantly, leading to a maximum temperature increase of 2.5 per cent, still four times smaller than in the 10s case discussed in Section 3.1. Moreover, the thermodynamic feedback remained insufficient to alter the cross-field Alfvén speed profile, limiting all phase mixing and dissipation to the initial shell region. Further increasing the viscosity significantly dampened the driven Alfvén waves, decreasing the available wave energy and therefore reducing the total coronal heating generated.

The imposed density gradients were relatively small so additional test simulations were performed which increased the initial cross-field density ratio between the interior and exterior from $\rho_i/\rho_e = 2.5$ to 4 and 10, strengthening the initial Alfvén gradient profile (dashed black line in Fig. 7). As expected, the amount of heating increased as the density gradients increased, with a maximum temperature increase of 3 per cent in the 100 s case. In addition, strengthening the initial Alfvén gradient broadened the region of strong density gradients ($|\frac{\partial V_A}{\partial x}| < 1$, Fig. 7), effectively broadening the region where efficient dissipation can occur in the 100 s case. However, despite the increased dissipation and heating, the effect on the loop structure

remained minimal. Moreover, it has been shown that expanding the region where phase mixing occurs also increases the associated radiative losses, therefore the additional energy dissipated may not be useful for heating (see e.g. Pagano & De Moortel 2017, 2019). These test cases indicate that the size of the dynamic viscosity and initially imposed density gradient profile are not the limiting factors preventing strong heating from occurring in the low-frequency cases. Instead it is likely the relative inefficiency of the phase mixing of low-frequency waves, in conjunction with the absence of wave energy trapping and subsequent temporal phase mixing that prevents the dissipation of low-frequency waves from acting as an efficient heating mechanism in these simulations.

In conclusion, our model describes a coronal loop within a semirealistic 2D atmosphere where we study the heating and evaporation caused by the dissipation of Alfvén waves. We find that high frequency waves can be efficiently dissipated, and that there is sufficient thermodynamic feedback to alter the loop structure, potentially enhancing the phase mixing process although the loop structuring is only maintained because of the presence of substantial background heating. On the contrary, energy carried by low-frequency waves is minimally retained by the corona despite the presence of the steep TR gradients and the dissipation by phase mixing is not otherwise efficient enough to provide significant heating.

DATA AVAILABILITY

The data from the numerical simulations and analysis presented in this paper are available from the corresponding author upon reasonable request.

REFERENCES

Antolin P., Okamoto T. J., De Pontieu B., Uitenbroek H., Van Doorsselaere T., Yokoyama T., 2015, ApJ, 809, 72
Arber T., Longbottom A., Gerrard C., Milne A., 2001, J. Comput. Phys., 171, 151
Arregui I., 2015, Phil. Trans. R. Soc. A, 373, 20140261
Berghmans D., de Bruyne P., 1995, ApJ, 453, 495
Bradshaw S. J., Cargill P. J., 2013, ApJ, 770, 12
Cargill P., Warren H., Bradshaw S., 2015, Phil. Trans. R. Soc. A, 373, 20140260
Cargill P., De Moortel I., Kiddie G., 2016, ApJ, 823, 31
De Moortel I., Nakariakov V. M., 2012, Phil. Trans. R. Soc. A, 370, 3193
De Pontieu B., Martens P., Hudson H., 2001, ApJ, 558, 859
Heyvaerts J., Priest E. R., 1983, A&A, 117, 220
Hinode Review Team K. et al., 2019, PASJ, 71, R1
Hollweg J. V., 1984, ApJ, 277, 392
Howson T. A., Breu C., 2023, MNRAS, 526, 499
Howson T., De Moortel I., 2023, Physics, 5, 140
Howson T., De Moortel I., Reid J., Hood A., 2019, A&A, 629, A60
Jess D. B. et al., 2016, Nat. Phys., 12, 179
Johnston C., Bradshaw S., 2019, ApJ, 873, L22
Johnston C., Hood A., Cargill P., De Moortel I., 2017, A&A, 605, A8
Johnston C. D., Hood A. W., De Moortel I., Pagano P., Howson T. A., 2021, A&A, 654, A2

Klimchuk J. A., 2015, Phil. Trans. R. Soc. A, 373, 20140256

Klimchuk J., Patsourakos S., Cargill P., 2008, ApJ, 682, 1351

Lionello R., Linker J. A., Mikić Z., 2009, ApJ, 690, 902

McIntosh S. W., De Pontieu B., Carlsson M., Hansteen V., Boerner P., Goossens M., 2011, Nature, 475, 477

McMurdo M., Ballai I., Verth G., Alharbi A., Fedun V., 2023, ApJ, 958, 81

Mikić Z., Lionello R., Mok Y., Linker J. A., Winebarger A. R., 2013, ApJ, 773, 94

Ofman L., Klimchuk J., Davila J., 1998, ApJ, 493, 474

Ofman L., Wang T., Davila J. M., 2012, ApJ, 754, 111

Okamoto T. J., Antolin P., De Pontieu B., Uitenbroek H., Van Doorsselaere T., Yokoyama T., 2015, ApJ, 809, 71

Pagano P., De Moortel I., 2017, A&A, 601, A107

Pagano P., De Moortel I., 2019, A&A, 623, A37

Pagano P., De Moortel I., Morton R., 2020, A&A, 643, A73

Parnell C. E., De Moortel I., 2012, Phil. Trans. R. Soc. A, 370, 3217

Reid J., Threlfall J., Hood A. W., 2023, MNRAS, 518, 1584

Ruderman M. S., Petrukhin N. S., 2017, A&A, 600, A122

Srivastava A. K. et al., 2021, J. Geophys. Res.: Space Phys., 126, e029097

Van Damme H., De Moortel I., Pagano P., Johnston C. D., 2020, A&A, 635, A174

Van Doorsselaere T. et al., 2020, Space Sci. Rev., 216, 1

Weberg M. J., Morton R. J., McLaughlin J. A., 2018, ApJ, 852, 57

Winebarger A., Tripathi D., Mason H. E., Del Zanna G., 2013, ApJ, 767, 107

Zhou Y.-H., Ruan W.-Z., Xia C., Keppens R., 2021, A&A, 648, A29

This paper has been typeset from a TEX/LATEX file prepared by the author.